The k-L turbulence model for describing buoyancy-driven fluid instabilities

VINCENT P. CHIRAVALLE

Los Alamos National Laboratory, Los Alamos, New Mexico

Abstract

The *k-L* turbulence model, where *k* is the turbulent kinetic energy and *L* represents the turbulent eddy scale length, is a two-equation turbulence model that has been proposed to simulate turbulence induced by Rayleigh-Taylor (RT) and Richtmyer Meshkov (RM) instabilities, which play an important role in the implosions of inertial confinement fusion (ICF) capsule targets. There are three free parameters in the *k-L* model, and in this paper, I calibrate them independently by comparing with RT and RM data from the linear electric motor (LEM) experiments together with classical Kelvin-Helmholtz (KH) data. To perform this calibration, I numerically solved the equations of one-dimensional (1D) Lagrangian hydrodynamics, in a manner similar to that of contemporary ICF codes, together with the *k-L* turbulence model. With the three free parameters determined, I show that the *k-L* model is successful in describing both shear-driven and buoyancy-driven instabilities, capturing the experimentally observed separation between bubbles and spikes at high Atwood number for the RT case, as well as the temporal mix width recorded in RM shock tube experiments.

Keywords: 1D Lagrangian hydrodynamics; Inertial confinement fusion; Numerical methods; Rayleigh Taylor instabilities; Turbulence modeling

1. INTRODUCTION

Over the past two decades, experiments with various inertial confinement fusion (ICF) capsule targets have shown that fluid instabilities play an important role in determining the efficiency of target implosion and the resulting neutron yield. There are three kinds of fluid instabilities of interest, Rayleigh-Taylor (RT), Richtmyer-Meshkov (RM), and Kelvin-Helmholtz (KH) instabilities. The Rayleigh-Taylor instability is driven by buoyancy at a perturbed interface between two fluids when the overall pressure and density gradients are opposite, such as when a light fluid decelerates a heavy fluid. The Richtmyer-Meshkov instability occurs when a shock interacts with a perturbed fluid interface. An impulsive drive is provided where the pressure and density gradients are misaligned, whether the shock passes from the light to heavy fluids or vice versa. The Kelvin-Helmholtz (KH) instability is driven by a velocity shear and can occur in a single fluid with homogeneous material properties.

Among these three kinds of instabilities, RT is especially important during the stagnation phase of an ICF implosion.

Experimental data and three-dimensional (3D) numerical simulations (Marinak *et al.*, 1996) indicate that the neutron yield of an ICF target capsule varies as the surface roughness of the inner shell of the capsule varies, because the level of RT turbulence that is induced during the implosion varies. Both data and simulation show a substantial decrease in the neutron yield with increasing level of RT turbulence. It is essential to model this effect in realistic computer simulations for ICF targets. Since it is impractical to numerically model the turbulence directly using a 3D simulation in all but a few cases, there exists a need for a comprehensive turbulence model that can be added to the contemporary one-dimensional (1D) Lagrangian, radiation-hydrodynamics codes that are widely used to design ICF target capsules (Haan *et al.*, 1995; Dittrich *et al.*, 1999; Peterson *et al.*, 2002) to capture the relevant physics of the non-linear stage of fluid instabilities.

Several empirical turbulence models have been proposed for simulating ICF implosions (Scannapieco & Cheng, 2002; Tipton, 1999; Youngs, 1989). Among these the *k-L* turbulence model (Tipton, 1999) has been used to study the performance of a double-shelled target capsule for **NIF** in 1D (Amendt *et al.*, 2002); however uncertainty exists as to how the empirical constants in this model should be chosen

---

and what their respective values should be. The goal of this paper is to present a methodology for determining the three empirical parameters in the *k-L* model, so that agreement is achieved with results from recent RT and RM experiments in addition to classical KH experiments involving the growth of shear mixing layers. Before describing the *k-L* model, my effort to calibrate it, and its ability to model relevant experiments, it is instructive to review a few of the many previous works involving RT, RM, and KH instabilities.

Among the earliest experimental work involving RT instability in fully non-linear regime was that of Read (1984). This series of experiments involved accelerating a container holding two incompressible, immiscible fluids, using a rocket attached to the container. It was shown that the light fluid (ρ_2) penetrates the heavy fluid (ρ_1) according to a square-law in time,

$$h_B = \alpha_B A g t^2, \tag{1}$$

where A is the Atwood number $((\rho_2 - \rho_1)/(\rho_2 + \rho_1))$, g is the constant acceleration of the fluid interface, and α_B is an empirical constant of roughly 0.05. In subsequent work, Dimonte and Schneider (2000) used a linear electric motor (LEM) in place of a rocket, to impart acceleration to a fluid interface, and they report that $\alpha_B = 0.05 \pm 0.005$ for bubbles over a range of Atwood numbers from 0.15 to 0.96. While the value of α_B is relatively constant, for the spike penetration where the heavy fluid penetrates the lighter fluid, it is shown that α_S is a function of density ratio, $R = \rho_2/\rho_1$ such that $\alpha_S = 0.05 R^{D_\alpha}$, where $D_\alpha = 0.33 \pm 0.05$ (Dimonte & Schneider, 2000).

In addition to studying RT instabilities with the LEM, Dimonte and Schneider (2000) also explore non-linear RM instabilities in the incompressible limit. In this case the bubble penetration length is found to obey a power-law relationship in time,

$$h_B = h_{B0} \left(\frac{u_0 t}{h_{B0} \theta_B} + 1 \right)^{\theta_B}, \tag{2}$$

where $\theta_B = 0.25 \pm 0.05$ and, like the RT case, the spike penetration length varies with density ratio such that $\theta_S = 0.25 R^{D_\theta}$, where $D_\theta = 0.21 \pm 0.05$. Other researchers have studied RM instabilities in the non-linear regime experimentally by considering the interaction of a shock wave with a fluid interface. Brouillette (2002) provides a comprehensive review of this field.

The above discussion has focused on RT and RM instabilities, with regards to shear instabilities, such as KH, there have been many extensive studies of this phenomenon experimentally and theoretically, and for this reason only, a brief review is given here. In general terms, a shear flow arises when there is a sharp velocity gradient separating two regions of flow, which may or may not have the same density. As time develops, if one moves in the frame with the average velocity of the flow, Brown and Roshko (1974)

show that for a uniform density flow, the mixing layer grows linearly in time such that

$$\delta = 0.18 \Delta v t, \tag{3}$$

where Δv is the initial velocity difference. Slessor *et al.* (2000) compiled all the available experimental data for the growth rate of compressible shear layers, and Speziale (1991) gives an excellent review of the $k - \varepsilon$, two-equation turbulence model which has found widespread application in the field of turbulence modeling using the Reynolds averaged navier-stokes (RANS) equations. This paper explores the use of the *k-L* turbulence model, in the context of a RANS-like approach, to model buoyancy and shear driven instabilities.

Several analytical models have been put forward, in addition to purely numerical simulations (Youngs, 1994; Marinak *et al.*, 1996; Holmes *et al.*, 1999; Weber *et al.*, 2003), to describe the non-linear turbulence induced by RT and RM instabilities. Among these models the buoyancy-drag (BD) model (Dimonte, 2000) has been the subject of much research, with various versions appearing in the literature. In its basic form, the model consists of two differential equations that describe the time evolution of the bubble and spike penetration lengths,

$$\frac{dL_k}{dt} = V_k, \tag{4}$$

$$\frac{dV_k}{dt} = C_B A g - C_D \frac{\rho_k}{\rho_s + \rho_b} \frac{V_k^2}{L_k}, \tag{5}$$

where L_k, V_k, and ρ_k represent the penetration length, velocity and density, respectively, of bubbles or spikes. C_B and C_D are empirical factors. There are two contributions to the penetration growth rate in this model, buoyancy being the first contribution, and drag the second. This model has been shown to give excellent agreement with the LEM experimental data (Dimonte & Schneider, 2000) for both the constant (RT) and impulsive (RM) acceleration cases.

This paper is organized as follows. In Section 2, I give a detailed description of the *k-L* turbulence model, which shares many features with the BD model discussed above. I also discuss my numerical implementation of the *k-L* model together with the equations of 1D Lagrangian hydrodynamics. The *k-L* model has three free parameters and next, in Sections 3, 4, and 5, I calibrate these parameters with existing experimental data from the LEM and shear flow experiments. In Section 6, I use the calibrated model to explore the variation of α_B and θ_B with Atwood number, and I compare the model results with data from the LEM. Following this I simulate two separate RM shock-tube experiments (Vetter and Sturtevant, 1995; Poggi *et al.*, 1998) in Section 7, where I compare the predicted total mix width as a function of time with the experimentally determined val-

ues in both cases. Finally, I end with a summary and conclusions.

2. MODEL DESCRIPTION

The *k-L* turbulence model attempts to capture the physics of the BD model where there is a turbulent eddy scale length equation and a turbulent velocity scale or growth rate equation. Whereas the BD model is purely zero-dimensional, the *k-L* model is a part of a larger 1D Lagrangian formulation. In such situations, each zone on the physical grid has its own value of eddy length scale and turbulent kinetic energy, unlike the BD model where there is one value of these quantities for the entire grid. The challenge in implementing a BD type model into a hydrodynamics code is how to use the values of length scale and turbulent kinetic energy to find the physical fluxes of species mass fraction, internal energy and momentum, which represent the turbulence that one attempts to model. The approach used by Tipton (1999) in the *k-L* model is to use the turbulent length and kinetic energy scales to construct an eddy viscosity, μ_t. This viscosity is then used to compute the turbulent fluxes of species mass fraction, *X* and internal energy, *e*. In addition, like the standard *k*-epsilon model (Speziale, 1991); widely used in shear flow problems, there is turbulent diffusion of length scale and turbulent kinetic energy in the *k-L* model as well.

Having outlined the basic features of the *k-L* model, I now present the full formulation as applied to an unsteady 1D problem where there are only variations in the spatial dimension *x*. I have included two velocity components, the velocity in the *x* direction, denoted as *u*, and the velocity in the transverse direction, denoted as *v*, so that I can model shear flow problems. The basic conservation equations for mass, momentum, internal energy, and species mass fraction, written in Lagrangian form, are as follows:

$$\frac{D\rho}{Dt} = -\rho \frac{\partial u}{\partial x}, \tag{6}$$

$$\rho \frac{Du}{Dt} = \frac{\partial}{\partial x}[-P + \tau_{xx}] + \rho g, \tag{7}$$

$$\rho \frac{Dv}{Dt} = \frac{\partial \tau_{xy}}{\partial x}, \tag{8}$$

$$\rho \frac{De}{Dt} = -P \frac{\partial u}{\partial x} + \frac{\partial}{\partial x} \mu_t \frac{\partial e}{\partial x} - \rho S_k, \tag{9}$$

$$\rho \frac{DX}{Dt} = \frac{\partial}{\partial x} \mu_t \frac{\partial X}{\partial x}. \tag{10}$$

In the above equations the total derivative, $D/Dt = \partial/\partial t + u(\partial/\partial x)$, is used corresponding to a reference frame moving with the fluid. In the equation for the *u* velocity, a body force term, ρg is included which will prove useful later when

modeling RT problems, and P is the total fluid pressure. The components of the Reynolds stress tensor, τ_{xx} and τ_{xy}, take the following form in the *k-L* model:

$$\tau_{xx} = -\frac{2}{3} \rho k + \frac{4}{3} \mu_t \frac{\partial u}{\partial x}, \tag{11}$$

$$\tau_{xy} = \mu_t \frac{\partial v}{\partial x}. \tag{12}$$

The eddy viscosity is determined by the turbulent length scale, *L*, and kinetic energy, *k*, according to the relation:

$$\mu_t = C_T \rho L \sqrt{2k}. \tag{13}$$

The equations that describe the time evolution of the *L* and *k* variables are given below:

$$\rho \frac{DL}{Dt} = \frac{\partial}{\partial x} \mu_t \frac{\partial L}{\partial x} + \rho S_L, \tag{14}$$

$$\rho \frac{Dk}{Dt} = \left[\tau_{xx} \frac{\partial u}{\partial x} + \tau_{xy} \frac{\partial v}{\partial x} \right] + \frac{\partial}{\partial x} \mu_t \frac{\partial k}{\partial x} + \rho S_k. \tag{15}$$

The source term for the production of the turbulent eddy scale length is as follows:

$$S_L = \sqrt{2k} + L \frac{\partial u}{\partial x}. \tag{16}$$

Turbulent eddy scale length is produced by two mechanisms, growth due to the turbulent kinetic energy represented by the $\sqrt{2k}$ term, and growth due to the compression of the flow, represented by the $L(\partial u/\partial x)$ term.

The source term for the production of the turbulent kinetic energy is as follows:

$$S_k = \sqrt{2k} \left\{ C_B Aa - \frac{C_D k}{L} \right\}. \tag{17}$$

In the above equation, *A* is the Atwood number and *a* is the local acceleration of the flow, $a = -(1/\rho)(\partial P/\partial x)$. There are two contributions to the production of turbulent kinetic energy that due to buoyancy effects, represented by the $C_B Aa$ term, and that is due to drag effects, represented by the $C_D k/L$ term.

Here I present a short summary of the numerical approach I used to implement the *k-L* model for 1D Lagrangian hydrodynamics; complete details are given elsewhere (Chiravalle, 2004). The general Lagrangian technique I used to solve the hydrodynamic equations above follows that presented by Bowers and Wilson (1991) and incorporates both a spatially and temporally staggered grid. In this Lagrangian formulation, the hydrodynamic equations are advanced explicitly in time by first solving the flow velocity

equations, Eq. (7) and Eq. (8), and then the x position of each zone boundary is updated. The new flow velocities are then used to find the velocity gradients and to update the turbulent length and kinetic energy scales. I update the length scale and turbulent kinetic energy equations, Eq. (14) and Eq. (15) by using the method of operator splitting. The effects due to the buoyancy-driven source term, S_k, the turbulent diffusion, and the shear-driven source term, $[\tau_{xx}(\partial u/\partial x) + \tau_{xy}(\partial v/\partial x)]$, are considered as three separate partial steps, performed in sequence. For the first partial step involving the buoyancy-driven source term, I used the two-stage predictor-corrector method (Tannehill *et al.*, 1997) to do the partial update. When I performed the partial update for the turbulent diffusion effects, I also performed the partial update on the mass fraction and internal energy equations as well. After fully updating Eq. (14) and Eq. (15), I then computed a new density for each cell, using the new zone widths and the constant mass of each zone. Following this, I solved for the internal energy, Eq. (9). At this point, I computed the new values of pressure and the Reynolds stress tensor as well as the new values of the time step to be used in the next cycle. I used a von Neumann formulation of artificial viscosity (Bowers & Wilson, 1991) to ensure numerical stability.

A central issue in implementing the *k-L* model numerically is the definition and computation of the Atwood number. I adopt the procedure developed by Tipton (1999). As part of this procedure at each zone boundary two densities, ρ_H and ρ_L, are defined such that

$$\rho_H = \rho_+ + \frac{dx}{2}\left(\frac{\partial\rho}{\partial x}\right)_{MONO+}, \tag{18}$$

$$\rho_L = \rho_- - \frac{dx}{2}\left(\frac{\partial\rho}{\partial x}\right)_{MONO-}. \tag{19}$$

In these equations, the subscript $+$ denotes the value at the zone center immediately to the right of the boundary, and the subscript $-$ denotes the corresponding value immediately to the left. For all the zones in the domain the monotonic density gradient, $(\partial\rho/\partial x)_{MONO}$, is calculated at zone center using the method of Van Leer (1977). The Atwood number at each zone boundary is computed then as

$$A = \frac{\rho_H - \rho_L}{\rho_H + \rho_L} + \frac{\langle L\rangle}{\langle\rho\rangle}\frac{d\rho}{dx}, \tag{20}$$

where $\langle L\rangle$ and $\langle\rho\rangle$ are the average values of the length scale and density at the zone boundary, and $d\rho/dx$ is the density derivative at the boundary, computed in the normal way. By computing A in this manner, both continuous and discontinuous effects at the zone boundaries are taken into account, as the first and second terms on the right-hand side of Eq. (20), respectively. In order to calculate the source terms, S_k and S_L, the Atwood number at the zone centers is needed, which

is obtained by simply taking the maximum value from both of the boundaries.

In total, there are three free parameters in the *k-L* model, C_B, C_D, and C_T. I used three test problems to calibrate these parameters independently: a shear layer growth test case, described in Section 3, a constant g (RT) test case, described in Section 4, and impulsive buoyancy (RM) test case, described in Section 5. The procedure for calibrating the model involves two steps; Step 1 entails calculating the shear layer growth and the impulsive buoyancy test problems using a wide range of values for C_D and C_T to determine which values match certain experimental data. The value of C_B is then determined in Step 2 by performing a series of calculations involving the constant g test case and comparing with data from the LEM.

3. SHEAR FLOW TEST PROBLEM

The shear layer growth problem involves an initial discontinuity in the v velocity at the origin as shown in Figure 1. The v velocity at the left hand boundary, denoted as v_L, is equal to 0.078 cm/μs and the initial velocity difference at the origin is $\Delta v = 0.031$ cm/μs. The pressure and density were held fixed everywhere else in the domain at 0.0172 Mbar and 1 g/cm^3, respectively. The u velocity was initially set to zero everywhere as well. As with all the problems considered in this paper, ideal gas equation of state is used and $\gamma = 1.4$, expect for the shock tube problems, discussed in Section 7. In this shear flow test problem, there is no distinction between the microscopic fluid properties on either side of the origin as there is in the two test problems to follow. This type of 1D shear flow problem has been used previously by Youngs (1994) to calibrate his multi-phase turbulence model.

For this kind of shear layer problem, the total width of the shear layer, δ, should grow linearly in time with a slope equal to $\delta' = 0.18\Delta v$ as discussed in Section 1. A complete analysis of the shear flow problem is given in this section,
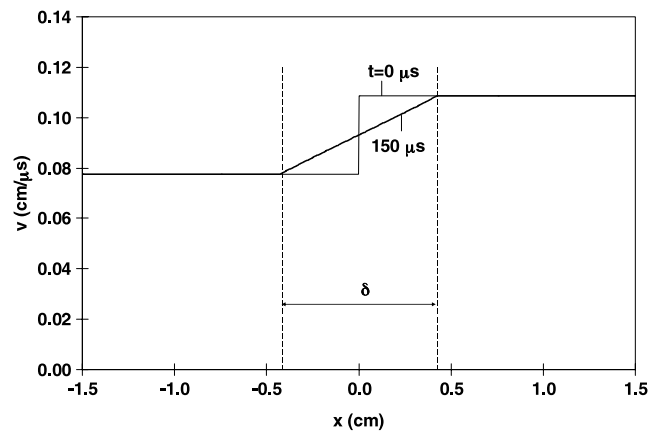

Fig. 1. Setup for the shear flow test problem, showing the v velocity profile at late time and how δ is calculated, for $C_D = 2.55$ and $C_T = 0.30$.
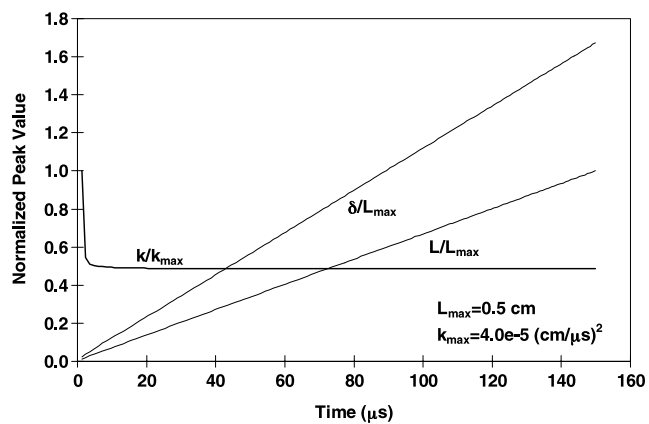
Fig. 2. Time plot of δ and the peak values of k and L for $C_D = 2.55$ and $C_T = 0.30$.

illustrating the important features of the problem including how δ is calculated, for the case where $C_D = 2.55$ and $C_T = 0.30$. Following this, a parameter study is performed where δ' is determined as a function of C_D and C_T.
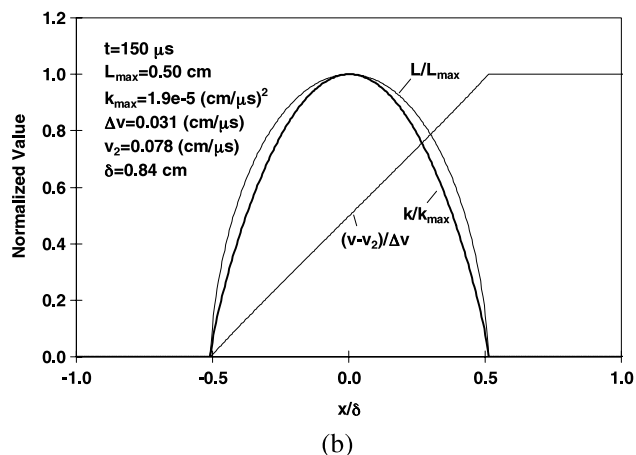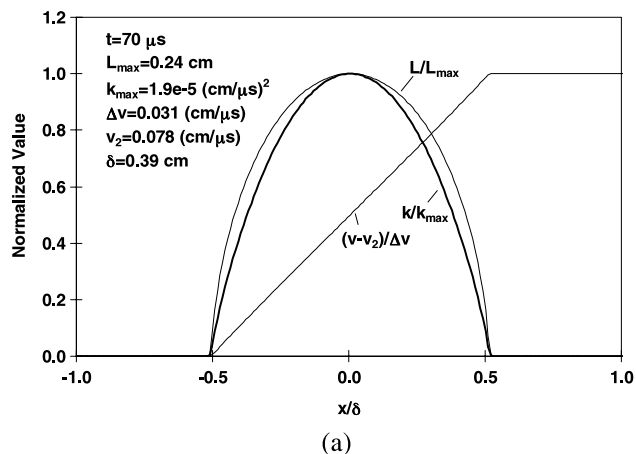

(a)

(b)

Fig. 3. Normalized profiles of v, L and k at 70 μs (a) and 150 μs (b) for $C_D = 2.55$ and $C_T = 0.30$.

The v velocity profile after 150 μs is shown in Figure 1, for the case where $C_D = 2.55$ and $C_T = 0.30$. For the shear flow test problem, the mix width, δ, is calculated as the distance between the two points corresponding to 99% and 1% of the velocity difference, Δv, as indicated in Figure 1. δ grows linearly in time, as shown in Figure 2, where it is evident that the peak value of the turbulent eddy length scale does also. The peak value of the turbulent kinetic energy approaches a constant value after a transient period of about 5 μs, also shown in Figure 2. The peak values are determined by finding the maximum values of the respective quantities over the entire domain at any given instant in time. The profiles of L and k, normalized by their peak values, are presented in Figure 3 at 70 and 150 μs, as functions of x/δ. Included also in Figure 3 is the v velocity profile, normalized by $(v - v_L)/\Delta v$. The normalized profiles of all three of these quantities are nearly identical at the two times shown, illustrating the self-similar nature of the problem.

As part of the calibration procedure, I show in Figure 4 the contours of normalized shear growth rate, $\delta'/0.18\Delta v$, as a function of C_D and C_T, for the shear flow test problem. The growth rate, δ', was determined numerically for each pair of C_D and C_T values by fitting a line, $c_1 + \delta' t$, to the calculated function of δ versus t, using a linear least-squares algorithm (Press *et al.*, 1992). A total of 400 pairs of C_D and C_T values where used to generate the contours in Figure 4. The contours are approximately straight lines, with C_T increasing as C_D increases for a given value of normalized growth rate. The contour of unity represents the experimental data of Brown and Roshko (1974), who report an experimental error of 10%.
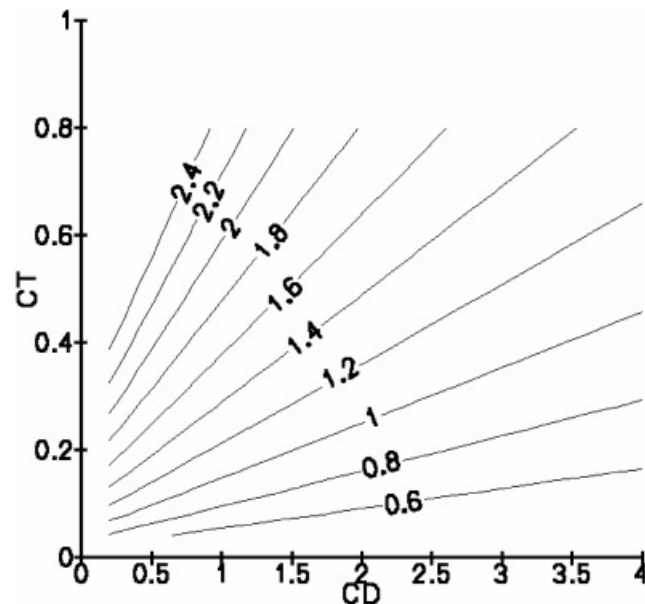

Fig. 4. Contours of normalized shear growth rate, $\delta'/0.18\Delta v$, for different values of C_D and C_T.

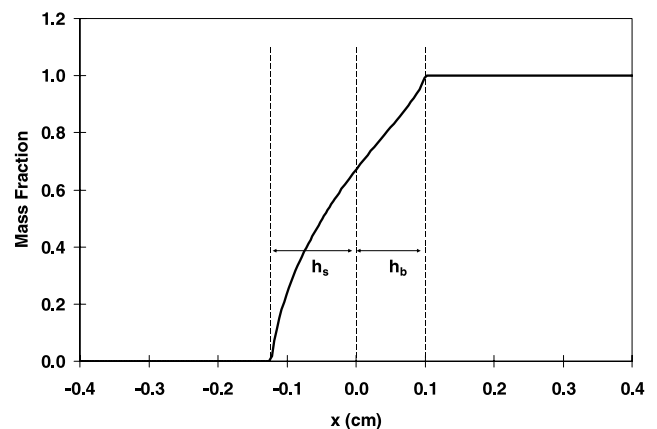## 4. IMPULSIVE TEST PROBLEM

The impulsive buoyancy test problem involves simulating a situation where the buoyancy term in S_k is suddenly brought to zero. Such a situation commonly occurs when a shock wave passes through a fluid interface, or when a large impulsive acceleration is applied to the interface, as realized in some of the LEM experiments. One way to approximate an impulsive buoyancy situation is to start a calculation with finite values of both k and L, generated for instance by running a constant g RT unstable problem for some length of time, and to turn off the buoyancy term in the model by setting $C_B = 0$. Without buoyancy, the penetration lengths should grow as a power-law in time according to Eq. (2), and the turbulent kinetic energy should decay monotonically in time. In this section, I describe in detail the results from an impulsive buoyancy test problem with $C_D = 2.55$ and $C_T = 0.30$, where I show how the bubble and spike penetration lengths, h_B and h_S, vary in time as well as the peak values of k and L. After this, I show how θ_B varies with C_D and C_T, completing Step 1 of the calibration procedure.
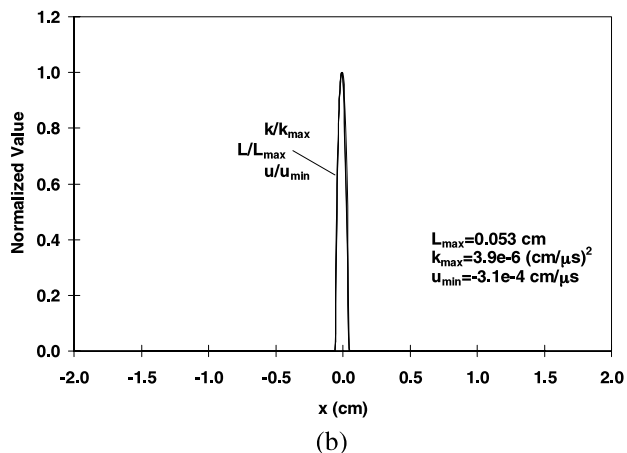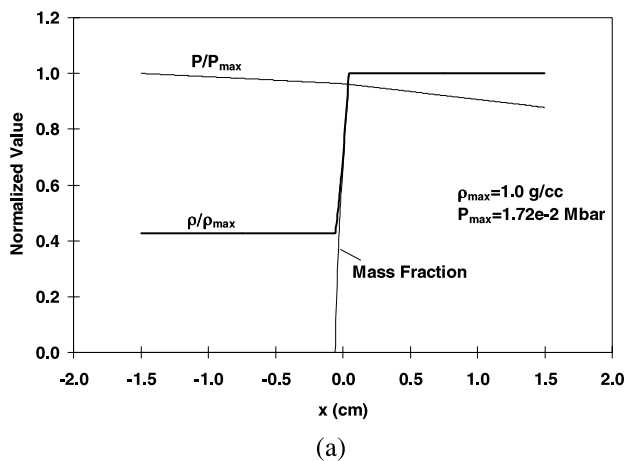
The initial conditions for the impulsive buoyancy test problem are shown in Figure 5. For this problem the Atwood number is 0.4. The finite pressure gradient which is evident in Figure 5 is maintained by applying a constant g of -9.8 cm/μs^2 throughout the duration of the calculation. Because $C_B = 0$ at all times, the pressure gradient does not produce any buoyancy in the problem. The mass fraction profile after 250 μs is shown in Figure 6. The bubble penetration length, h_B, is defined in this paper as the distance between the origin and the point where the mass fraction is 99%, as illustrated in Figure 6. Similarly the spike penetration length, h_S, is defined as the distance between the origin and 1% mass fraction point, also shown in Figure 6. Both h_S and h_B grow in time according to Eq. (2), with $\theta_S = \theta_B = 0.25$, as indicated in Figure 7. θ_S and θ_B are determined by fitting a function, $c_1(1 + c_2 t)^\theta$, to the calculated penetration lengths. The fits for bubbles and spikes that were used to determine θ_B and θ_S are shown in Figure 7. A non-linear Levenberg-Marquardt fitting algorithm (Press *et al.*, 1992) was used to find the parameters, c_1, c_2 and θ, for each fit. Figure 7 also reveals that the peak value of k decays monotonically in time and the corresponding value of L grows according to a power law, in the same fashion as h_S and h_B. The spatial profiles of mass fraction, k, and L, normalized by their peak values, are given at 125 and 250 μs in Figure 8. Once again when appropriately normalized these profiles are essentially the same at early and late times.

Figure 9 shows the contours of θ_B as a function C_D and C_T, and as in Figure 4, 400 pairs of C_D and C_T values were used to generate the contours in Figure 9. In most of the domain, there is virtually no dependence on C_T. It seems that θ_B depends almost entirely on the value of C_D, decreasing inversely with C_D. The impulsive LEM experiments obtain $\theta_B = 0.25 \pm 0.05$ and to match this result requires that $C_D = 2.55$. With this value of C_D the contours of Figure 4 indicate that C_T must be equal to 0.30 to match the Brown and Roshko (1974) experimental result for the shear growth rate. This completes Step 1 of the calibration procedure.

(a)

(b)

Fig. 5. Setup for the impulsive buoyancy test problem. The normalized values of pressure, density, and the mass fraction profile are shown in (a) at $t = 0$, and the corresponding values of k, L and u are shown in (b).

Fig. 6. Mass fraction profile at 250 μs for the impulsive buoyancy test problem with $C_D = 2.55$ and $C_T = 0.30$.
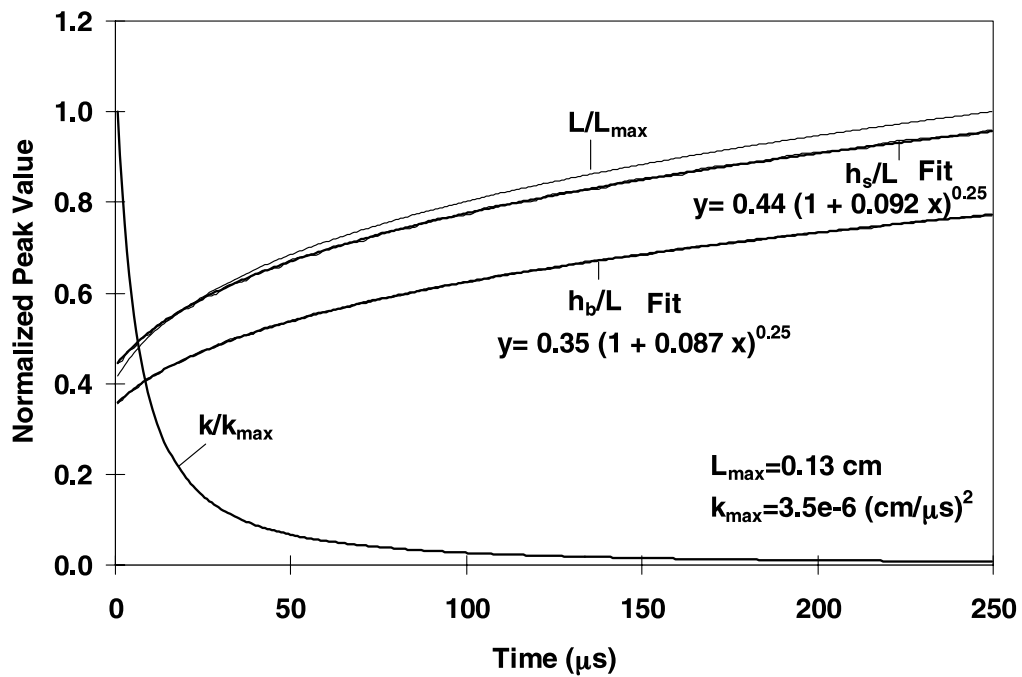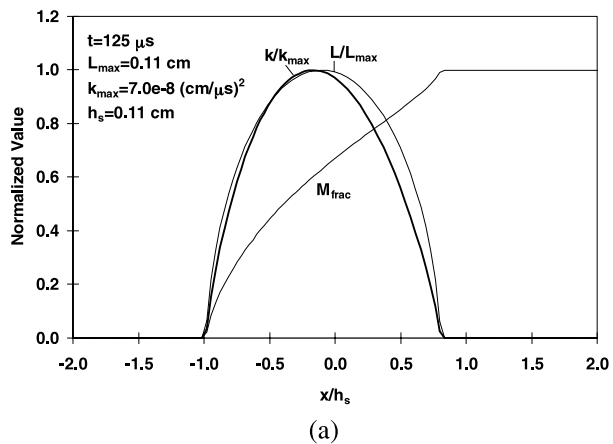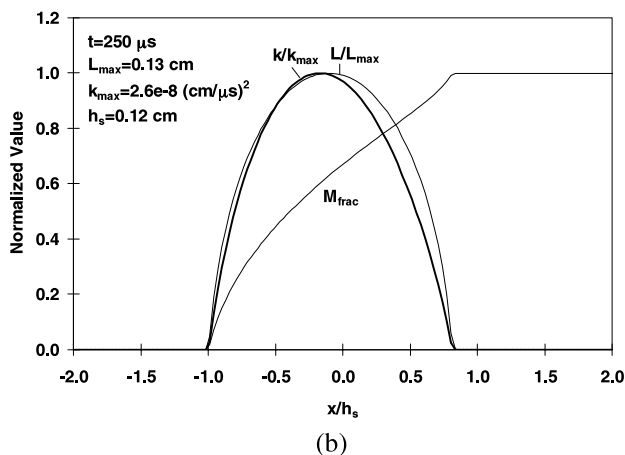
Fig. 7. Time evolution of h_S and h_B and the peak values of L and k with $C_D = 2.55$ and $C_T = 0.30$.

(a)

(b)

Fig. 8. Normalized profiles of L, k and mass fraction at 125 μs (a) and 250 μs (b).

5. CONSTANT g TEST PROBLEM

With C_D and C_T determined from Step 1, the value of C_B is now fixed in Step 2 by considering a constant g RT unstable test problem. For this test problem at $t = 0$, there is a discontinuity in density of 0.67 g/cm^3, corresponding to an Atwood number of 0.5, at the origin, and the density and pressure gradients have opposite signs, as shown in Figure 10. Initially the flow is in hydrostatic equilibrium with a
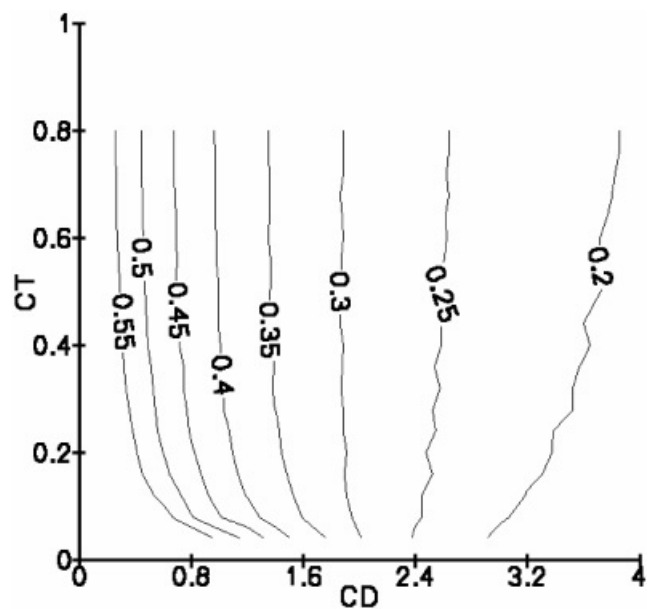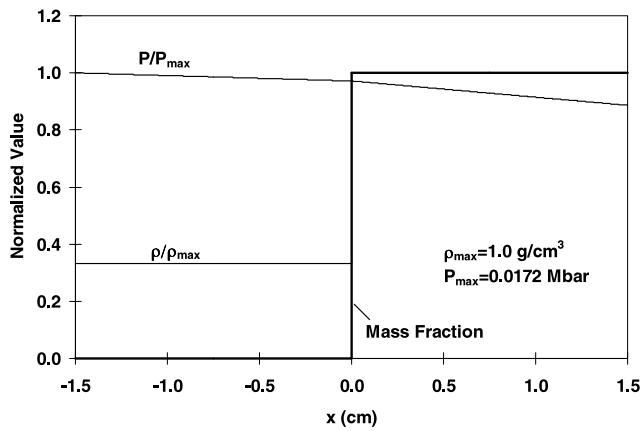

Fig. 9. θ_B versus C_D and C_T.

Fig. 10. The initial pressure and density profiles in the constant g test problem.

constant g field, equal to -9.8×10^{-4} cm/μs^2, which remains fixed throughout the calculation. The initial velocity is zero everywhere, as is the initial turbulent kinetic energy. The initial value of turbulent eddy scale length is set to 10^{-7} cm everywhere, except in the cells before and after the boundary between heavy and light fluids. In these two cells, the turbulent eddy scale length is taken to be 10^{-3} cm. Under such conditions the bubble and spike penetration lengths should grow in a self-similar way, according Eq. (1), once the instability has outgrown the initial linear phase. In this section, I present first the complete analysis of this RT unstable problem with $C_B = 1.20$ and then later I show how α_B varies with C_B.

The bubble and spike penetration lengths as a function of time are given in Figure 11, for the constant g test problem with $C_B = 1.20$. The same definition of bubble and spike penetration lengths that was used in the impulsive buoyancy problem and illustrated in Figure 6 is also used here. To determine the values of α_B and α_S, I fit the function, $c_1 + \alpha A |g| t^2$, to the calculated penetration lengths, using a least-squares fitting routine (Press *et al.*, 1992) to find the two parameters c_1 and α. I include the fitted functions for both bubble and spike penetration lengths in Figure 11, where it is evident that in both cases t^2 behavior is predicted by the model, with $\alpha_B = 0.05$ and $\alpha_S = 0.07$. Also from Figure 11 it is clear that the peak values of both k and L exhibit t^2 behavior as well. In Figure 12, the spatial profiles of the mass fraction and, k and L, normalized by their peak values, are given at 70 and 140 μs, as a function of x/h_S, and the self-similar nature of this test problem is evidenced. The Atwood number profile at 140 μs, computed using Eq. (20), is given in Figure 13 and it is interesting to note that the peak value at 140 μs is about 20% larger than the initial, prescribed value of 0.5. In determining α_B and α_S through the fitting routine, the initial prescribed value of the Atwood number, 0.5, is used.

In Figure 14, I show α_B as a function of C_B, as determined using the constant g test problem, and the same analysis described above. Twenty points were used to generate the profile in Figure 14. To achieve agreement with the LEM result of $\alpha_B = 0.05 \pm 0.005$, it is necessary to have $C_B = 1.20$. Now that I have calibrated all three of the free parameters in the k-L model, I can explore how the model performs at various Atwood numbers, and its ability to simulate the interaction of a shock wave with a fluid interface.
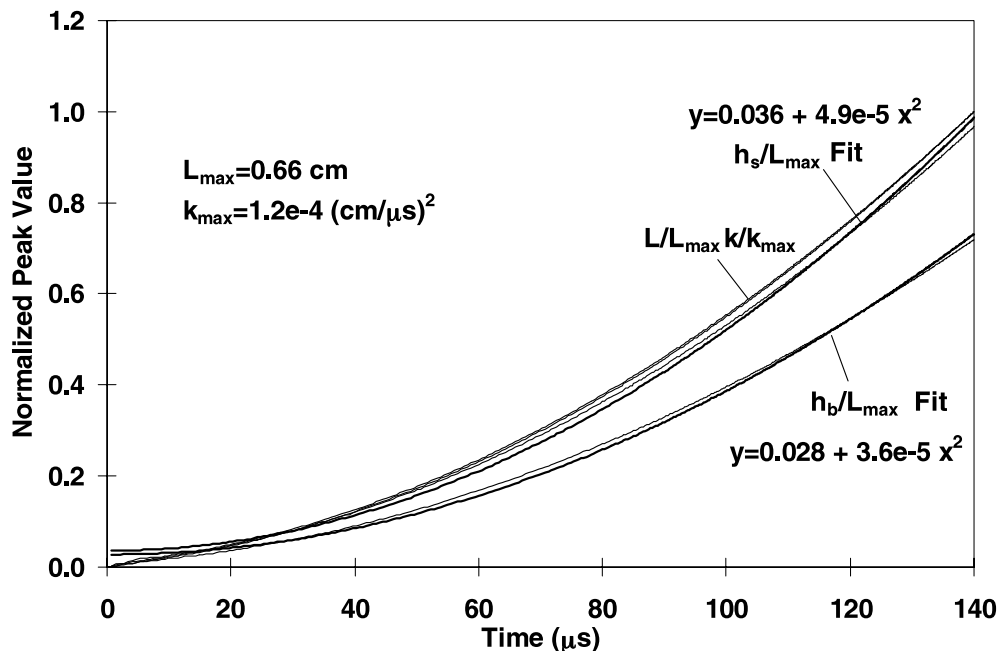

Fig. 11. Time evolution of h_S and h_B, and the peak values of L and k for the constant g test problem with $C_B = 1.20$.
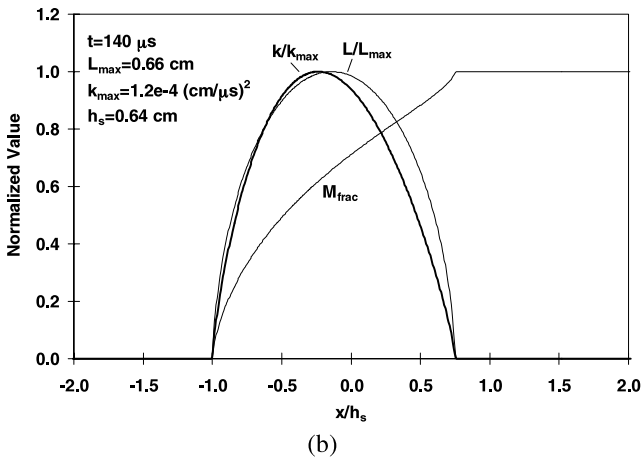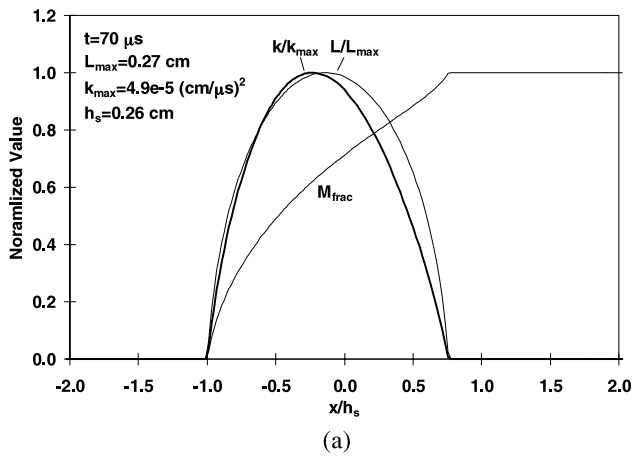
(a)

(b)

Fig. 12. Normalized profiles of *L*, *k* and mass fraction at 70 μs (a) and 140 μs (b) for $C_B = 1.20$.

6. EFFECT OF ATWOOD NUMBER ON θ_B AND α_B

In this section, a study is made using the test problems from the previous two sections, to evaluate the effect of Atwood
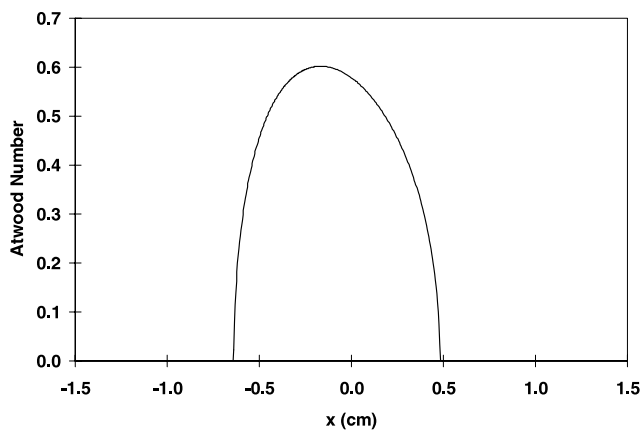

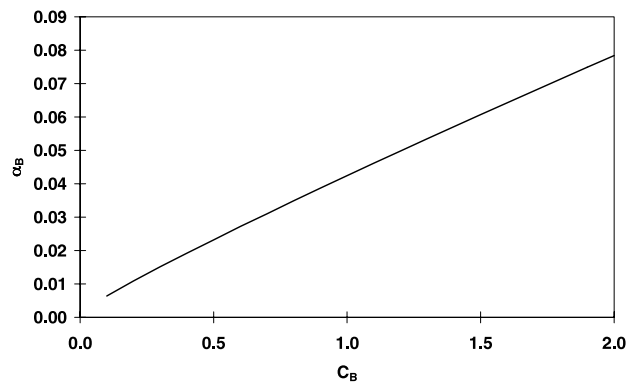**Fig. 13.** The Atwood number profile at 140 μs, computed using Eq. 20.

Fig. 14. α_B versus C_B for the constant *g* test problem.

number on θ_B and α_B as predicted by the *k-L* model. There exists a comprehensive set of data from the LEM, involving constant *g* and impulsive buoyancy situations, over a wide range of Atwood numbers. I will compare the results of the *k-L* model to this data. In doing so, I must point out that the LEM experiments were conducted primarily using liquids, not gases, as is the case with the test problems I use in this paper. I have already used some of the LEM data in the calibration procedure, and in doing so I have assumed that the behavior of θ_B and α_B, as observed during the LEM experiments, is the same for any two materials undergoing turbulent mixing regardless of the form of their equations of state. This point remains to be established experimentally however. In this section, I first present the results of the impulsive buoyancy test problem for a variety of Atwood numbers, and I compare θ_B and θ_S from the *k-L* model with the LEM data in each case. This is then followed by the corresponding results for the constant g RT unstable test problem.

In Figure 15, the predicted values of θ_B and θ_S from the *k-L* model are shown together with the corresponding LEM data over a range of Atwood numbers from 0.05 to 0.95. The model predictions in Figure 15 were generated by running
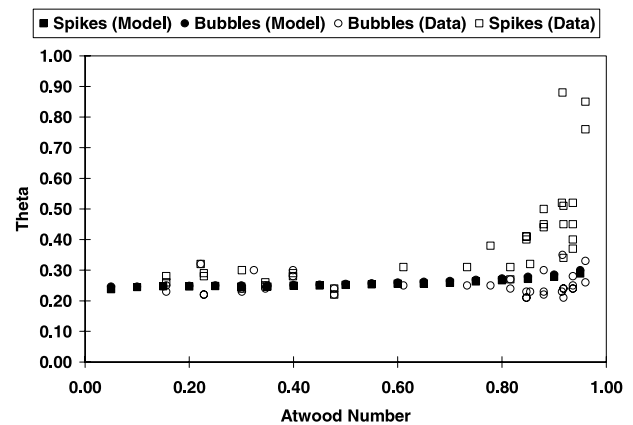

Fig. 15. θ_B and θ_S versus Atwood number. The corresponding LEM data (Dimonte & Schneider, 2000) are shown as open symbols.
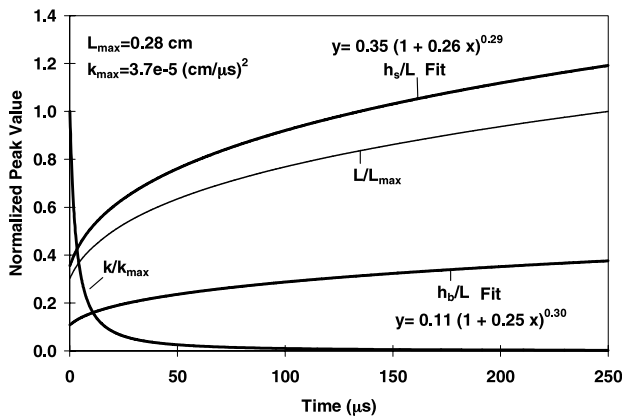
Fig. 16. Time evolution of h_S and h_B, and the peak values of L and k for the impulsive buoyancy test problem at an Atwood number of 0.95.

the impulsive buoyancy test problem for a series of different Atwood numbers. I initialize the computation for each of the different cases using profiles similar to those depicted in Figure 5, taking into account the appropriate density difference needed to achieve the prescribed global value of the Atwood number. The prescribed global Atwood number, used in Figure 15, is specified in terms of the densities at the left and right most points on the grid and is not related to the Atwood number for each zone, as computed by Eq. (20) during the calculation. As seen in Figure 15, the model

predicts little variation in θ_B with Atwood number, as observed in the LEM experiments. In addition, the model suggests that there is little difference between θ_B and θ_S, with both being about 0.25. The LEM experiments show that θ_B and θ_S are the same at low Atwood number, but when the Atwood number exceeds about 0.7, the data suggests a separation between the two, although there is a noticeable spread in the data. The *k-L* model does not predict a clear difference between θ_B and θ_S in this regime. A time history of the bubble and spike penetration lengths for the impulsive buoyancy test problem at the highest Atwood number considered, 0.95, is given in Figure 16. The spike penetration length is about three times greater than the corresponding bubble length, but yet the model predicts that θ_B and θ_S are about the same.

In Figure 17, α_B and α_S are shown, as calculated by the *k-L* model for the constant g test problem, over a range of Atwood numbers from 0.05 to 0.95. The corresponding LEM data is also shown for comparison. The model predicts that α_B is relatively constant everywhere at 0.05. Unlike the impulsive buoyancy test problem, at high Atwood number, the model does show a definite separation between α_B and α_S for the constant *g* test problem, for instance at an Atwood number of 0.95 α_S is about 3.1 times larger than α_B which is in good agreement with the LEM data. A complete time history for the calculation at 0.95 is given in Figure 18. The bubble and spike penetration lengths are shown to increase smoothly in time, proportional to t^2, as expected.
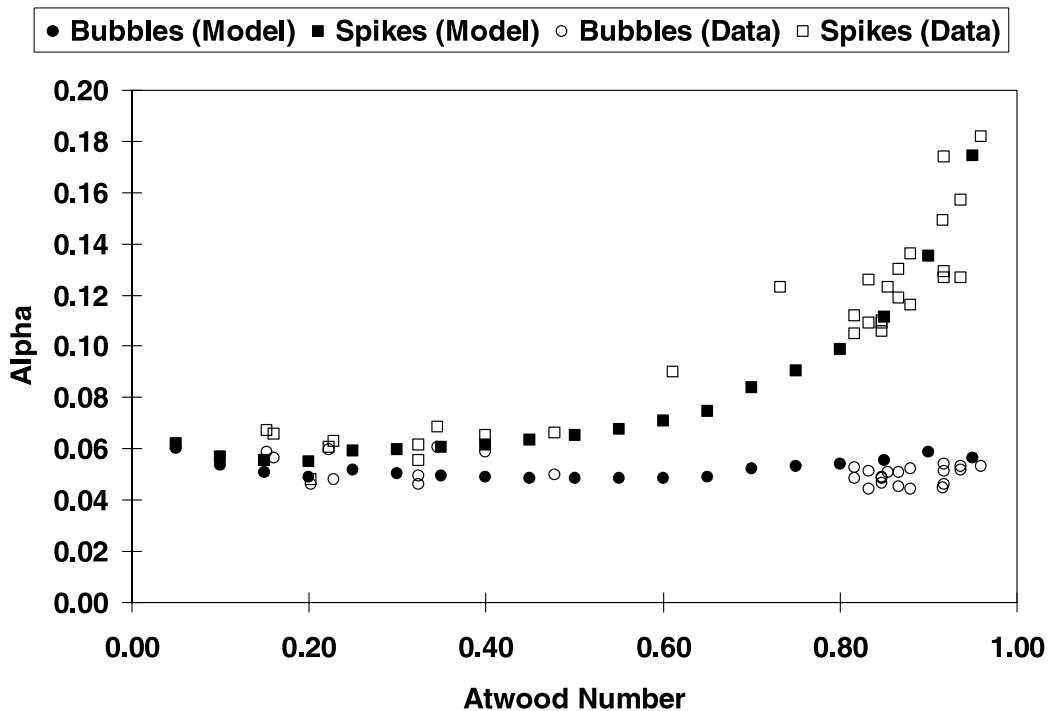

Fig. 17. α_B and α_S versus Atwood number. The corresponding LEM data (Dimonte & Schneider, 2000) are shown as the open symbols.
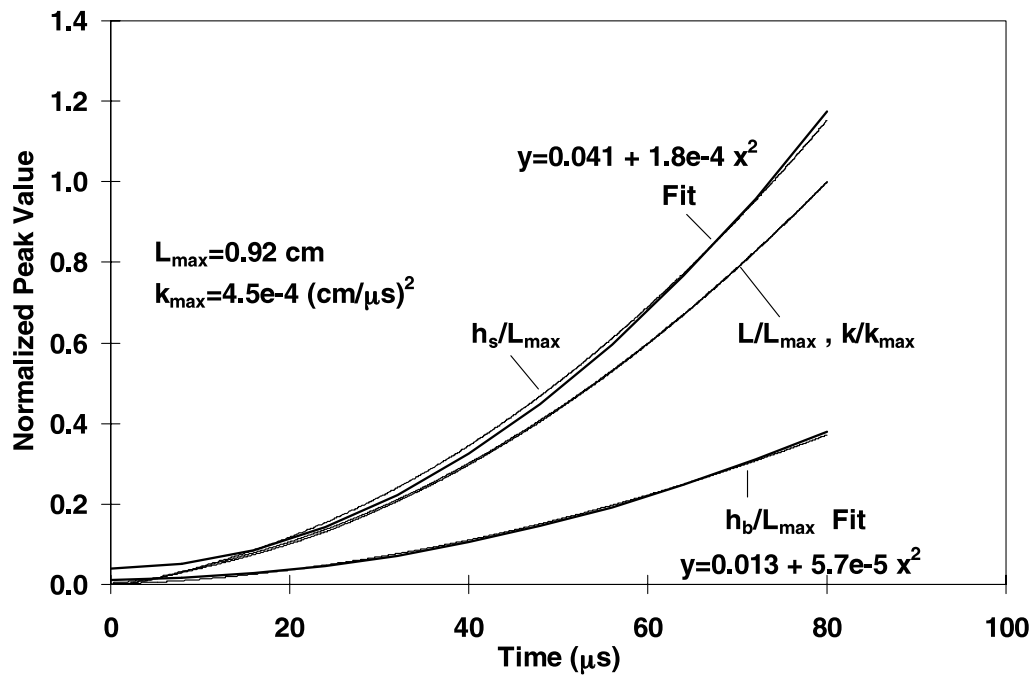
Fig. 18. Time evolution of h_S and h_B, and the peak values of L and k for the constant g test problem at an Atwood number of 0.95, with $C_B = 1.20$.

7. SHOCK-TUBE PROBLEMS

I now use the *k-L* model to simulate two shock-tube experiments (Vetter & Sturtevant, 1995; Poggi *et al*., 1998), both of which involve situations where in addition to the initial interaction there is a second shock interaction with the interface involving the reflected shock from the wall of the shock-tube. In both cases, experimental data for the total width of the turbulent mixing layer was obtained as a function of time, using a schlieren technique to image the flow. It is important to note that RM type instabilities occur regardless of the sign of $\nabla \rho \cdot \nabla P$ at the interface, and the two experiments that I chose to simulate represent both of these scenarios. Each of the two shock tube experiments involves a fluid interface consisting of air and SF_6. For both cases, an initial shock wave of roughly $M = 1.45$ is generated in the tube and travels through the fluid interface, then reflects off the end wall of the test section, and interacts with the fluid interface again. In the case of Vetter and Sturtevant (1995), the reflected shock travels through SF_6 and $\nabla \rho \cdot \nabla P > 0$ at the interface, whereas for that of Poggi *et al*. (1998), the reflected shock travels through air and $\nabla \rho \cdot \nabla P < 0$.

When simulating these experiments numerically, I take $\gamma = 1.095$ for SF_6 and $\gamma = 1.4$ for air. I initialize the turbulence parameters in the same way as for the constant g test problem, except that I consider values of initial eddy scale length, L_0, other than 10^{-3} cm in the two cells adjacent to the fluid interface. It is necessary to do this in order to match the experimental data for the total mix width, and a direct measurement of the initial eddy length scale is not viable.

First I simulate the experiment of Poggi *et al*. (1998), involving multiple reflected shocks. To give an indication of when the reflected shocks interact with the fluid interface, I performed a calculation with no mix, and the location of the interface and the shock position are shown in Figure 19 as functions of time for this experiment. Including the effects of turbulent mix, I find that a value of 2 mm for L_0 leads to good agreement with the data in this case, as shown in Figure 20. The data exhibits two small dips in the mix width, which are also predicted by the model and apparently correspond to those times when a reflected shock interacts with
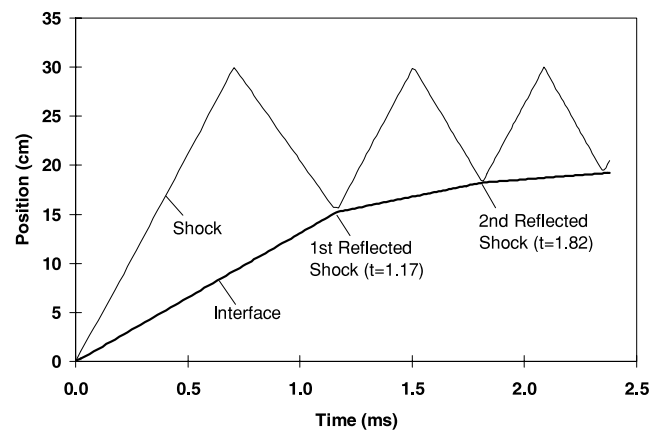

Fig. 19. Calculated position of the shock and the interface, without mix, as a function of time for the experiment of Poggi *et al*. (1998). The times when the reflected shock interacts with the interface are indicated in milliseconds.
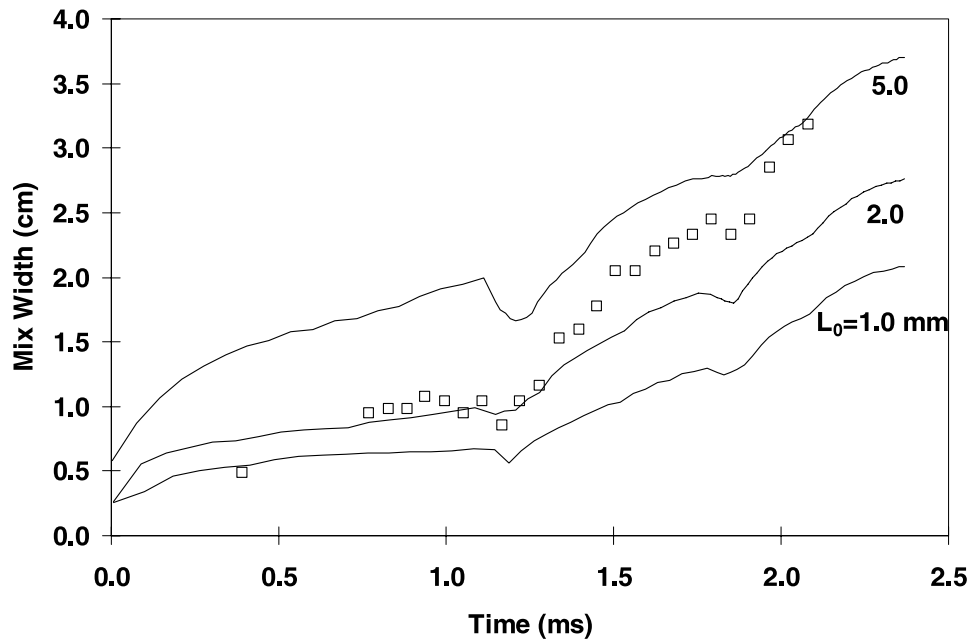
Fig. 20. Calculated mix width as a function of time for the experiment of Poggi *et al*. (1998). Their data are shown as the open symbols.

the interface at 1.17 and 1.82 ms as shown in Figure 19. These times also correspond closely to those temporal locations were the peak value of turbulent kinetic energy is large as shown in Figure 21. The model predicts that when the reflected shock interacts with the fluid interface turbulent kinetic energy is produced, and this energy is then slowly dissipated after the reflected shock passes through the interface. This is most clearly visible at about 1.17 ms in Fig-

ure 21. The peak turbulent eddy length scale increases at all times, also evident in Figure 21.

Figure 22 shows the time history of the total mix width predicted by the *k-L* model for the Vetter and Sturtevant (1995) experiment, together with their data. As the initial eddy scale length is reduced from 0.5 mm to 0.01 mm, satisfactory agreement is achieved with the data at initial times, between 2 and 3 ms, and at later times, between 4 and
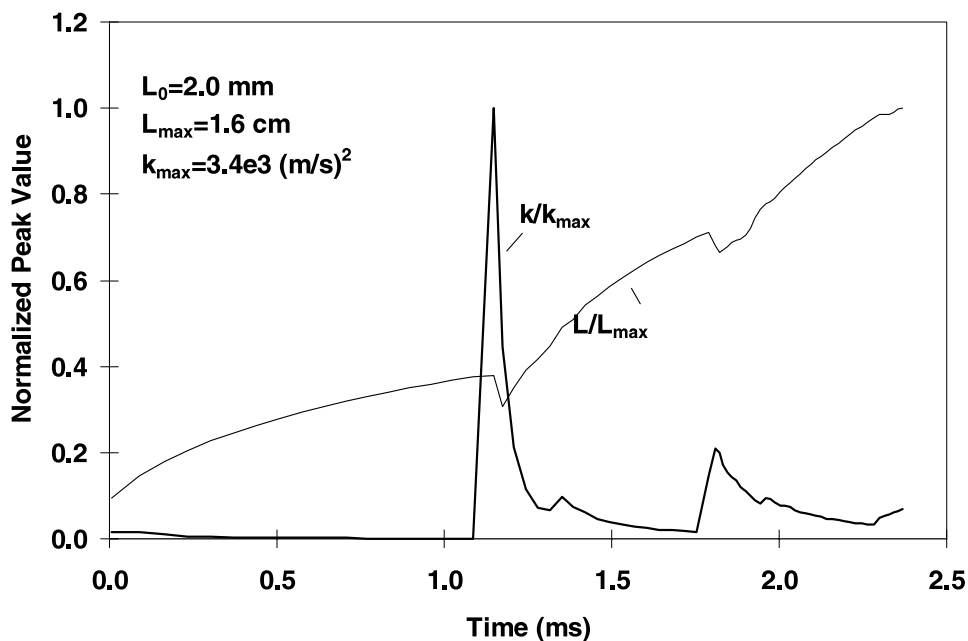

Fig. 21. Time evolution of the peak values of L and k, predicted by the *k-L* model with $L_0 = 2$ mm, for the experiment of Poggi *et al*. (1998).
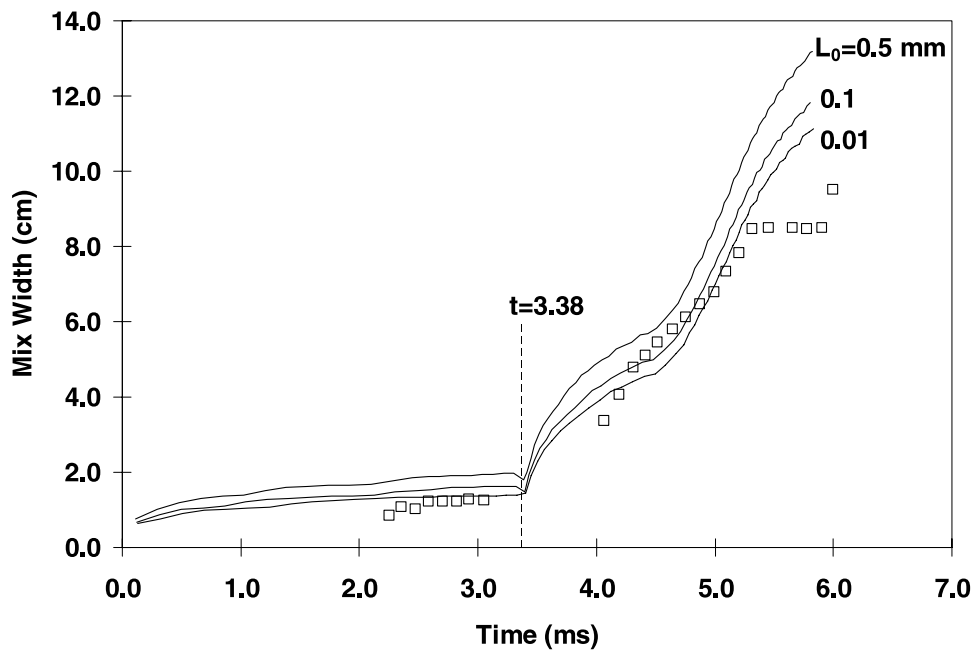
Fig. 22. Calculated mix width as a function of time for the Vetter & Sturtevant (1995) experiment. Their data are shown as the open symbols. The time when the reflected shock hits the interface (dashed line) is given in milliseconds.

5 ms, after the interaction with the reflected shock which takes place at 3.38 ms. However, adjusting L_0 alone can not reconcile the model with the data after 5 ms. The data shows a plateau in this region but the model gives a mix width that continues to grow. As with the experiment of Poggi *et al*. (1998), the model shows a sharp increase in turbulent kinetic energy when the reflected shock interacts with the interface at about 3.38 ms, and after this interaction the turbulent kinetic energy decays as illustrated in Figure 23.

5. SUMMARY AND CONCLUSIONS

In this paper, I explored three simple test problems, a constant g test problem, an impulsive buoyancy test problem, and a shear layer test problem, using the *k-L* turbulence model. By using data from the LEM experiments of Dimonte and Schneider (2000), and the shear layer mixing data obtained by Brown and Roshko (1974), I calibrated the three free parameters in the *k-L* model and found that $C_T = 0.30$, $C_D = 2.55$, and $C_B = 1.20$. Having calibrated the model several conclusions can be drawn regarding its ability to predict various characteristics of RT and RM instabilities

For the constant g RT test problem, the *k-L* model captures the t^2 dependence for the bubble and spike penetration lengths, and is successful in reproducing the behavior of α_B and α_S over the entire range of Atwood numbers as observed in the LEM experiments. For the impulsive buoyancy test problem, the *k-L* model predicts that both bubbles and spikes grow according to Eq. (2) with $\theta_B \approx \theta_S \approx 0.25$ over the complete range of Atwood numbers, and does not predict separation between θ_B and θ_S at high Atwood numbers,

as implied by the results from the LEM experiments. Future work must address this issue and perhaps some modification of the drag term in the standard *k-L* model may improve this situation. For both the RT and RM test problems, the *k-L* model shows the expected self-similar behavior at late times. When applied to the shear flow problem, the *k-L* model indicates that the turbulent kinetic energy should approach a constant value at late times, and both the turbulent eddy length and the width of the shear layer should grow linearly in time, in accordance with experiments.

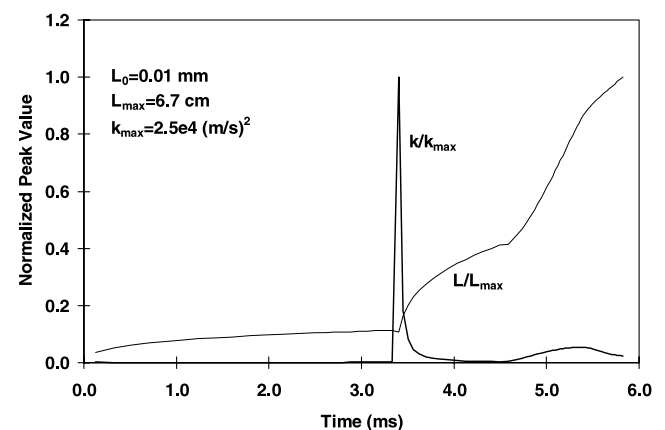With the proper adjustment of the initial turbulent eddy scale length, the *k-L* model is successful in capturing the

Fig. 23. Time evolution of the peak values of L and k, predicted by the *k-L* model with $L_0 = 0.01$ mm, for the experiment of Vetter & Sturtevant (1995).

essential features of the temporal development of the total mix width for the shock tube experiments of Vetter and Sturtevant (1995) and Poggi *et al.* (1998). In both cases, the model predicts that as the reflected shock hits the fluid interface, the turbulent kinetic energy increases sharply and then subsequently decays after the passage of the shock. However, the model is not successful in capturing the late-time behavior observed by Vetter and Sturtevant (1995). This point should be explored in future works. In this paper, only one data set from the Vetter and Sturtevant (1995) was used, it would be worthwhile to perform simulations for the other data sets they present as well.

Although more work remains to be done to improve the *k-L* model, this paper has shown that it is a robust turbulence model, that in addition to adequately dealing with shear-driven instabilities also embodies the physics of RM and RT instabilities in the fully non-linear regime. In the future, I hope to apply the *k-L* model to situations of relevance to ICF physics, and address its ability to predict the dynamics of hydrodynamic implosions.

ACKNOWLEDGMENTS

REFERENCES

AMENDT, P., COLVIN, J.D., TIPTON, R.E., HINKEL, D.E., EDWARDS, M.J., LANDEN, O.L., RAMSHAW, J.D., SUTER, L.J., VARNUM, W.S. & WATT, R.G. (2002). Indirect-drive noncryogenic double-shell ignition targets for the national ignition facility: Design and analysis. *Phys. Plasmas* **9**, 2221–2233.

BOWERS, R. & WILSON, J. (1991). *Numerical Modeling in Applied Physics and Astrophysics*. Boston: Jones & Bartlett Publishers.

BROUILLETTE, M. (2002). The Richtmyer-Meshkov instability. *Annu. Rev. Fluid Mech.* **34**, 445–468.

BROWN, G.L. & ROSHKO, A. (1974). On density effects and large structure in turbulent mixing layers. *J. Fluid Mech.* **64**, 775–816.

CHIRAVALLE, V.P. (2004). The implementation of the k-l turbulence model for buoyancy-driven instabilities in a 1Dlagrangian hydrocode. LA-UR-04-7626. Los Alamos, NM: Los Alamos National Laboratory.

DIMONTE, G. (2000). Span wise homogeneous buoyancy-drag model for Rayleigh-Taylor mixing and experimental evaluation. *Phys. Plasmas* **7**, 2255–2269.

DIMONTE, G. & SCHNEIDER, M. (2000). Density ratio dependence of Rayleigh-Taylor mixing for sustained and impulsive acceleration histories. *Phys. Fluids* **12**, 304–321.

DITTRICH, T.R., HAAN, S.W., MARINAK, M.M., HINKEL, D.E., POLLAINE, S.M., MCEACHERN, R., COOK, R.C., ROBERTS, C.C., WILSON, D.C., BRADLEY, P.A. & VARNUM, W.S. (1999). Capsule design for the national ignition facility. *Laser Part. Beams* **17**, 217–224.

HOLMES, R.L., DIMONTE, G., FRYXELL, B., GITTINGS, M.L., GROVE, J.W., SCHNEIDER, M., SHARP, D.H., VELIKOVICH, A.L., WEAVER, R.P. & ZHANG, Q. (1999). Richtmyer-Meshkov instability growth: Experiment, simulation and theory. *J. Fluid Mech.* **389**, 55–79.

HAAN, S.W., POLLAINE, S.M., LINDL, J.D., SUTER, L.J., BERGER, R.L., POWERS, L.V., ALLEY, W.E., AMENDT, P.A., FUTTERMAN, J.A., LEVEDAHL, W.K., ROSEN, M.D., ROWLEY, D.P., SACKS, R.A., SHESTAKOV, A.I., STROBEL, G.L., TABAK, M., WEBER, S.V., ZIMMERMAN, G.B., KRAUSER, W.J., WILSON, D.C., COGGESHALL, S.V., HARRIS, D.B., HOFFMAN, N.M. & WILDE, B.H. (1995). Design and modeling of ignition targets for the national ignition facility. *Phys. Plasmas* **2**, 2480–2487.

MARINAK, M.M., TIPTON, R.E., LANDEN, O.L., MURPHY, T.J., AMENDT, P., HAAN, S.W., HATCHET, S.P., KEANE, C.J., MCEAHERN, R. & WALLACE, R. (1996). Three-dimensional simulations of nova high growth factor capsule implosion experiments. *Phys. Plasmas* **3**, 2070–2076.

PETERSON, R.R., HAYNES, D.A., GOLOVKIN, I.E. & MOSES, G.A. (2002). Inertial fusion energy target output and chamber pressure response: Calculations and experiments. *Phys. Plasmas* **9**, 2287–2292.

PRESS, W.H., TEUKOLSKY, S.A., VETTERLING, W.T. & FLANNERY, B.P. (1992). *Numerical Recipes in C: The Art of Scientific Computing*. New York: Cambridge University Press.

POGGI, F., THOREMBEY M.H. & RODRIGUEZ, G. (1998). Velocity measurements in turbulent gaseous mixtures induced by Richtmyer–Meshkov instability. *Phys. Fluids* **10**, 2698–2700.

READ, K.I. (1984). Experimental investigation of turbulent mixing by the Rayleigh-Taylor instability. *Physica D* **12**, 45–48.

SCANNAPIECO, A.J. & CHENG, B. (2002). A multifluid interpenetration mix model. *Physics Lett. A.* **299**, 49–64.

SLESSOR, M.D., ZHUANG, M. & DIMOTAKIS, P.E. (2000). Turbulent shear-layer mixing: growth-rate compressibility scaling. *J. Fluid Mech.* **414**, 35–45.

SPEZIALE, C.G. (1991). Analytical methods for the development of Reynolds-stress closures in turbulence. *Annu. Rev. Fluid Mech.* **23**, 107–157.

TANNEHILL, J.C., ANDERSON, D.A. & PLETCHER, R.H. (1997). *Computational Fluid Mechanics and Heat Transfer*. Washington, DC: Taylor & Francis Publishers.

TIPTON, R.E. (1999). A phenomenological k-l mix model for NIF targets in 1, 2 and 3 dimensions. *Proc. 7th International Workshop on the Physics of Compressible Turbulent Mixing*, Sarov, Russia: RFNC-VNIIEF.

VAN LEER, B. (1977). Towards the ultimate conservative difference scheme III: Upstream-centered finite-difference schemes for ideal compressible flow. *J. Comp. Phys.* **23**, 263–275.

VETTER, M. & STURTEVANT, B. (1995). Experiments on the Richtmyer-Meshkov instability of an air/sf$_6$ interface. *Shock Waves* **4**, 247–252.

WEBER, S.V., DIMONTE, G. & MARINAK, M.M. (2003). Arbitrary lagrange-eulerian code simulations of turbulent Rayleigh-Taylor instability in two and three dimensions. *Laser Part. Beams* **21**, 455–461.

YOUNGS, D.L. (1994). Numerical simulation of turbulent mixing by Rayleigh-Taylor and Richtmyer-Meshkov instabilities. *Laser Part. Beams* **12**, 725–750.

YOUNGS, D.L. (1989). Modeling turbulent mixing by Rayleigh-Taylor instability. *Physica D* **37**, 270–287.